Advanced method to derive the IMF direction near Mars from cycloidal proton distributions

M. Yamauchi[1], Y. Futaana[1], A. Fedorov[2], E. Kallio[3], R. A. Frahm[4], R. Lundin[1], J.-A. Sauvaud[2], J.D. Winningham[4], S. Barabash[1], and M. Holmström[1]

1 Swedish Institute of Space Physics, Box 812, S-98 128, Kiruna, Sweden
2 Centre d'Etude Spatiale des Rayonnements, BP-4346, F-31028 Toulouse, France
3 Finnish Meteorological Institute, Box 503 FIN-00101 Helsinki, Finland
4 Southwest Research Institute, San Antonio, TX 7228-0510, USA

Abstract

In a previous paper, we showed a method for deriving the interplanetary magnetic field (IMF) orientation from the velocity distribution of ring-like distributed ions as measured by the Ion Mass Analyser (IMA) on board Mars Express (MEX). This method has been improved so that one can derive the IMF orientation from a very limited portion of the ring distributions, i.e., only the highest energy portion of the ring distribution. This method uses the maximum variance direction **L** instead of the minimum variance direction **N**, which are derived from manually selected ring data. Because IMA's count rate for a semi-persistent ring distribution is nearly proportional to energy squire, **L** is most likely aligned to the tangential direction of the ring distribution at its highest energy, and this tangential direction is parallel or anti-parallel to the electric field. A vector product of **L** and the solar wind direction (X) gives the IMF orientation projected to the Y-Z plane. The tilt angle of IMF toward the X direction from the Y-Z plane is the same as the angle between the X direction and the ring plane, and is obtained from two methods when the initial speed of the ring ions is estimated to be much smaller than the solar wind speed: (1) angle between the velocity of ring's maximum energy portion and the solar wind vector, and (2) energy ratio between the solar wind and the maximum energy of the ring. The present method is applied to the IMA data from 3 June 2005 (0605 - 0640 UT) when the Mars Global Surveyor (MGS) magnetometer data is available. Using this data, we also tried to determine the sign of the IMF direction by estimating the evolution direction of the ring ions.

Keyword: IMF, Mars, ion gyration, ring distribution

(Yamauchi, et al., Planet. Space Sci., 56(8), 1145-1154, doi:10.1016/j.pss.2008.02.012, 2008.)

1. Introduction

The European Space Agency's Mars Express (MEX) spacecraft carries the Analyzer of Space Plasma and EneRgetic Atoms (ASPERA-3) experiment that measures hot plasma and energetic neutral atoms (Barabash et al., 2006), but MEX does not carry a magnetometer. Magnetic field orientation is absolutely necessary in interpreting the ASPERA-3 data. Therefore, we have developed a method to derive the interplanetary magnetic field (IMF) orientation (except for its sign) from the velocity distribution of ring-like ions measured by the Ion Mass Analyzer (IMA) in a previous paper (Yamauchi et al., 2006; hereafter called Paper 1).

In Paper 1, we used the fact that the magnetic field direction in velocity space is the same in the Martian frame and in the solar wind frame, and that newly born ions make a simple circular trajectory around the IMF in velocity space. By determining the best-fit plane in velocity space that arranges ions with the same initial velocity in a circle, we estimated the IMF orientation as the normal direction of this ring plane. The best-fit plane is determined by the minimum variance method in which the maximum variance direction (**L**), medium variance direction (**M**), minimum variance direction (**N**) of the manually selected ring data from the IMA data are calculated in velocity space. **L** and **M** compose the best-fit plane in velocity space, and hence **N** is a good estimate of the IMF orientation with an ambiguity of sign. Both newly ionized neutrals and reflected solar wind, which are observed upstream of the Martian bow shock, can be used for our purpose.

The problems with this method are that (1) we have to manually select a "clean" data set that is only composed of ring ions with the same initial velocity, and (2) IMA is not optimized to detect the ring distribution for both angular resolution and energy range (Paper 1). While IMA has 6°~7° angular resolution in the elevation direction, it only has 22.5° angular resolution in the azimuthal direction. Besides mass analyzer's low energy limit around 0.7 keV for protons (this was fixed by changing bias voltage in 2007), the low flux of the ring protons (about 2% of the solar wind flux) makes them difficult to be detected at an energy less than about 1.5 keV because the IMA's count rate depends strongly on energy as is discussed in section 3.

Due to these instrumental limitations, we sometimes identify the ring ions in only a few directions when the ring plane is nearly aligned to IMA's azimuthal direction. In such cases, only the highest energy portion of the ring ions can be manually extracted from ions that belong to other phenomena. With such very limited data, the minimum variance method can only determine the **L** direction with a small ambiguity, but the derived **M** and **N** directions have large ambiguities. In this paper, we show an alternative method to overcome this ambiguity.

2. Instrument

The IMA instrument, a part of ASPERA-3 experiment on board MEX, is a top hat instrument that combines an electrostatic energy analyzer with a magnetic mass analyzer. IMA has a 4.6° × 360° field of view, where the 360° measurement plane is divided into 16 azimuthal sectors, each 22.5° wide. IMA has an extra electrostatic deflection system (or elevation analyzer) at its entrance, which scans from -45° to +45° (16 elevations) in approximately 3 min. The actual entrance angle of the ions is slightly energy dependent. The overall field-of-view is approximately 360° (16 sectors) × 90° (16 elevations). With this design, the angular resolution of IMA is greater in elevation than in azimuth; and therefore, the amount of uncertainty in the velocity measurement is less in the elevation direction than in the azimuthal direction.

IMA measures ions in the energy range from 10 eV/q to 30 keV/q in 96 logarithmically scaled energy steps every 12 sec. Since IMA's magnetic mass analyzer deflects sub-keV protons to the outside of its microchannelplate (MCP) sensor, the effective lower energy limit for protons is about 0.7 keV for a particular observational mode which optimizes proton observations. Above the lower energy limit, the count rate is nearly proportional to the differential energy flux density ($J_E(\varepsilon, \Omega)$, where ε is energy and Ω is solid angle) because the energy bandwidth of the electrostatic energy analyzer is nearly proportional to the energy for a particle instrument using an electrostatic energy analyzer. For details of the IMA instrument and its operational modes, see Barabash et al. (2006), Fedorov et al. (2006), and Paper 1.

3. Method

The principle of the present method is explained in Paper 1 (Figure 4). Here we look at the ring distribution around the IMF (**B**) in another way. Figures 1 and 2 illustrate the velocity space trajectories of ions with initial velocity $\mathbf{V}_0 = 0$ (ignorable compared to the solar wind velocity $\mathbf{V}_{SW}$) and with $\mathbf{V}_0 \neq 0$, respectively. The three directions (X, T, E) are defined such that X points in the $-\mathbf{V}_{SW}$ direction, E points in the $\mathbf{E}_{SW} = -\mathbf{V}_{SW} \times \mathbf{B}$ direction, and T completes the right-hand Cartesian coordinates; i.e., T points in the $\mathbf{E}_{SW} \times (-\mathbf{V}_{SW}) = (\mathbf{V}_{SW} \times \mathbf{B}) \times \mathbf{V}_{SW}$ direction. In this coordinate, $\mathbf{B}_T$ is the magnetic field component perpendicular to the solar wind direction ($B_T \geq 0$).

%%%%%% Figure 1 %%%%%%

Ions with zero initial velocity ($\mathbf{V}_0 = 0$) in Martian frame form a circular trajectory perpendicular to **B** with a radius of $|V_{SW}|\cos(\theta)$ as illustrated in Figure 1b, where θ is the angle between **B** and the V_T axis (i.e., $\sin(\theta) = B_X/|B|$). The circle is common for all protons with $\mathbf{V}_0 = 0$. For non-zero initial velocity ($\mathbf{V}_0 \neq 0$) cases such as the reflected solar wind (e.g. Sckopke et al., 1990), both the initial position and the radius of the ring

in velocity space are different from the zero initial velocity ($\mathbf{V}_0 = 0$) case, with the ring's radius of $|(\mathbf{V}_0-\mathbf{V}_{SW}) \times \mathbf{B}|/|B|$. However, the ring plane is still perpendicular to **B**. Therefore, by finding the coordinate that arranges these ions a circle in velocity space, we can in principle obtain the **B** (and hence $\mathbf{E}_{SW}$) orientations from the normal direction to the ring plane.

The question is then the procedure to find such a coordinate system (V_X, V_T, V_E), i.e., obtaining the ring plane orientation. In reality, the actual data, which is obtained with finite angular resolution, contains many ion counts related to different types of physics and different initial velocities ($\mathbf{V}_0$). Paper 1 dealt with relatively easy cases when (1) we can successfully create a clear set of data composed only of ions with the same $\mathbf{V}_0$ and (2) the circle is detected in a dense set of velocity space points, e.g., with 6°~7° angular resolution in the IMA's elevation scan direction. The latter (high angular resolution) is a tough condition because IMA has only 22.5° angular resolution in the azimuthal direction. Generally, distribution of the ring is not necessarily aligned in the elevation direction. While clear sets of ring data can be selected from 80% of bow shock traversals during the optimum operation mode, only one quarter of these clear sets of data are aligned in the elevation scan direction of IMA (see Paper 1).

To consider cases with low angular resolution, we have marked in Figures 1 and 2 possible velocity space points that can be detected by IMA when the ring distribution is aligned in the azimuthal direction. The hexagonal marks denote detectable velocity space points (center position) in the Martian frame with finite energy resolution (as marked by thin circles) and 22.5° angular resolution. The sequential numbers ("1" to "6") in Figure 1 represent the evolution of the ring (in the gyration direction). The size of these hexagonal marks represents the expected counts.

When the ring distribution is semi-persistent over a gyroperiod (i.e., decay is small), the phase-space density (distribution function *f*) is constant inside the ring distribution in velocity space in the solar wind frame. Unlike differential number flux density ($J(\varepsilon, \Omega) = v \cdot f(\mathbf{v}) dv^3/d\varepsilon d\Omega \propto \varepsilon \cdot f(\varepsilon, \Omega)$, where **v** is velocity) or differential energy flux density ($J_E(\varepsilon, \Omega) \propto \varepsilon^2 \cdot f(\varepsilon, \Omega)$), phase-space density *f* is conserved under Lorenz transform, i.e., it is constant inside the ring distribution even in the spacecraft frame of reference. Since IMA's count rate is nearly proportional to $J_E(\varepsilon, \Omega)$, the count rate for the ring distribution is nearly proportional to energy squire. This fact makes the highest energy portion (e.g., "4", "3", and "5" in Figure 1) be easily recognized as a part of the common ring distribution, while it makes the expected count of the low energy portion (e.g., "1" and "6" in Figure 1) be easily buried among other counts that belong to other phenomena. Furthermore, the low energy portion points in quite different direction from the highest energy portion in velocity space. Therefore, it is difficult to identify the low energy portion as the part of the same ring distribution as the high energy portion.

Let us consider the expected maximum, medium, and minimum variance directions (**L**, **M**, **N**, respectively) of these asymmetric data. The orientation of ±**N**, which is the best estimate of the IMF orientation, has the largest uncertainty in the **M** direction (Paper 1). If only 3 points ("4", "3", and "5" in Figure 1) are reliable, this uncertainty is severe such that using ±**N** as the orientation of the IMF is erroneous. For such worst scenarios, however, one can still use **L** as a good estimate of a vector that composes the ring plane. This is enough in order to determine the $\pm\mathbf{B}_T$ direction as described below.

%%%%%% Figure 2 %%%%%%

When the flux of the ring distribution does not change very much during its gyration, **L** is mainly determined by the highest energy portion of the ring distribution ("4", "3", and "5" in Figure 1) due to IMA's energy-dependent count rate, and hence, **L** is nearly aligned to the tangential direction of the ring at its highest energy point. For a cycloidal motion, the ion energy reaches its maximum when the electric field is perpendicular to the motion (i.e., at the turning direction where ion is accelerated to decelerated). This means that the tangential direction of the ring distribution at its highest energy point is anti-parallel to the solar wind electric field ($\mathbf{E}_{SW}$) in velocity space (see Figure 1a). This parallel geometry applies even to the ring trajectory of beam origin ($\mathbf{V}_0 \neq 0$) as illustrated in Figure 2. In Figure 2, two types of IMF conditions, (a) $|B_X| < B_T$, and (b) $< |B_X| > B_T$ (≥ 0), are illustrated to show that a large B_X does not change this difficulty/easiness in obtaining the ring plane. Therefore, **L** is a good estimate of the $\pm\mathbf{E}_{SW}$ directions, from which the $\mathbf{B}_T$ ($= \mathbf{V}_{SW} \times \mathbf{E}_{SW}/|E_{SW}|^2$) orientation can also be estimated.

The ring distribution is not always semi-persistent but it may change quickly due to scattering or sector anomaly etc.. In such variant cases, **L** is no longer parallel to $\pm\mathbf{E}_{SW}$. In the worst case, **L** can even be oriented perpendicular to the V_E axis like the **M** direction (using data points "3", "2", and "1") in Figure 1. In this case, the estimate of the V_E axis, and hence the $\mathbf{B}_T$ orientation, is 90° off from the actual orientation.

However, this type of failure can be avoided by examining the L_X component because L_X is expected to be small compared to the other components when **L** is nearly aligned to the V_E axis. If L_X is large (e.g., > 0.38 which corresponds to more than 22.5° offset, while > 0.20 corresponds to 11.25° offset), the low energy data (e.g., "6", "2" or "1" in Figure 1) must have been over-weighted in obtaining **L**. In this case, we should remove the point that caused such offset, i.e., the direction corresponding to the lowest energy from the selected data, until we find the "cleanest" data set that gives **L** nearly aligned to the tangential direction of the ring distribution at its highest energy. On the other hand, an asymmetric data (with large L_X) may contain evolution information of the ring distribution (e.g., by scattering). If one may estimate the evolution direction, that gives the sign of $\mathbf{E}_{SW}$ (and hence $\mathbf{B}_T$). We will discuss this using the real data in the next section.

Next, we consider the tilt angle θ of the IMF toward the V_X axis (or $\sin(\theta) = B_X/|B|$), which is identical to the tilt angle of the ring plane from the V_X-V_E plane, i.e., from the V_X axis (see lower panels of Figures 1 and 2). In the minimum variance method, the accuracy of the derived θ depends on the alignment of **M** in the ring plane, which has a large error bar when the orientation of the instrument relative to the ring plane is not ideal. However, we have other ways to derive θ if $|V_0|$ is small compared to $|V_{SW}|$. The methods are outlined in Paper 1 as the "intuitive method", in which the newly ionized hydrogen corona (i.e., $\mathbf{V}_0 = 0$) is found to be the largest source of the ring distribution.

If $\mathbf{V}_0 = 0$, there are two ways to obtain θ from the velocity space point exhibiting the highest energy of the ring distribution. In Figure 1b (lower panel), θ is identical to the tilt angle θ' between the direction of the highest energy of the ring distribution and $\mathbf{V}_{SW}$. At the same time, the diameter of the ring ($= 2V_{SW}\cos(\theta)$) is the same as the speed of the highest energy. Therefore, the highest energy ε_{MAX} is equal to $4\varepsilon_{SW}\cos^2(\theta)$, where ε_{SW} is the solar wind energy. As long as $|V_0| << |V_{SW}|$, both methods give quite reasonable estimates of θ.

For large $\mathbf{V}_0$, the deviation from θ becomes large for both methods in different ways, and hence, the differences between the two estimates becomes large. In other words, similarity of estimated angles between the two methods is a necessary condition in assuming $|V_0| << |V_{SW}|$. Other necessary conditions are also discussed in Paper 1: they are (a) low temperature (the spread in energy is very small at any given direction), and (b) the alignment in a circle that paths through zero velocity. The latter condition is the same as $\varepsilon_{MAX} = 4\varepsilon_{SW}\cos^2(\theta)$ condition for a linearly aligned case instead of a circle when the low-energy part of the ring distribution is not detected.

In summary, we have the following procedure for estimating the IMF orientation.
(1) Manually select the ring distribution, for which the spread in energy is very small in any given direction.
(2) Apply the minimum variance method to determine **L**, **M**, and **N**. If the ring data is well arranged into a partial circle which passes through zero velocity (in Martian frame) in the V_L-V_M plot, the deviation in the **N** direction must be small, and we use ±**N** as the magnetic field orientation. Details of this procedure, up to here, is described in Paper 1 (see also Sonnerup and Scheible (1998) for the minimum variance method).
If the above criterion (2) is not satisfied (i.e., if the estimated error in this method is more than 30°), we should not use **M** or **N**, and use the present method.
(3) Examine the orientation of **L** whether it is nearly perpendicular to $\mathbf{V}_{SW}$ (or $|L_X| < 0.3$ which corresponds to 17° offset). If so, **–L** is a good estimate of $\pm\mathbf{E}_{SW}$ (and hence V_E) direction. If not, remove the direction that corresponds to the lowest energy from the selected set of ring data and re-calculate a new **L**, until **L** becomes nearly perpendicular to $\mathbf{V}_{SW}$. If $|L_X|$ does not approach less than 0.3, either the selected distribution did not

originate from the same V_0 or $\mathbf{E}_{SW}$ changed significantly within a gyroperiod. One must also examine if the data is aligned in a partial ring or in a line in velocity space.
(4) Obtain ε_{MAX} and θ'. This can be done manually by looking at the selected ring data.
(5) Check if $\varepsilon_{MAX}/4\varepsilon_{SW} \approx \cos^2(\theta')$ is satisfied. If yes, and if the data is nearly linearly aligned, we may most likely assume $\theta \approx \theta'$, where $B_X/|B| = \sin(\theta)$.
(6) If possible, identify the evolution direction (e.g., by decay direction). That determines the sign of $\mathbf{L}$ and $\mathbf{E}_{SW}$. $\mathbf{B}_T$ is parallel to $\mathbf{V}_{SW} \times \mathbf{E}_{SW}$. This is discussed in the next section.

4. Example: 3 June 2005.

Here we apply the above method to the MEX/IMA data upstream of the bow shock flank during the outbound traversal on 3 June 2005 at around 0610 UT. We choose this period because the IMF estimation using the Mars Global Surveyor (MGS) magnetic field data exists (Acuna et al., 1998; Frilund et al., 2008).

Figure 3 shows the MEX orbit and energy-time spectrograms of the electron (ELS) and ion (IMA) data during 0545-0645 UT on 3 June 2005. The solar wind velocity is about 600 km/s (proton energy about 2 keV) during this period. All axes references are made with the Mars-Sun Orbit (MSO) Cartesian coordinate system, with the +X direction pointing sunward, the +Y direction duskward, and the +Z direction toward the north ecliptic pole, and $R^2 = Y^2+Z^2$.

The spacecraft traversed the bow shock on the dawn side of Mars (outbound) at around 0551 UT, as identified by the sudden change of the thermalization level of the solar wind (192 sec cycle regular pattern of most intense counts) and electrons as observed by both IMA and ELectron Spectrometer (ELS). Until the end of IMA operation (~0643 UT), the solar wind protons appeared at ~2 keV/q and alpha particle at ~4 keV/q in the middle of the IMA's elevation scan (elevation=6~8) every 192 sec (scanning cycle). In addition to them, IMA detected substantial counts in the southward looking elevation direction (elevation=10~15) at energies 2~10 times the energy of the solar wind proton until about 0633 UT, whereas no count is detected in the northward looking elevation direction (elevation=0~5). The low energy part of these extra counts (marked by circles) is a strong candidate for cycloidal proton distribution with $|V_0| << |V_{SW}|$. To further examine these counts, we plot the data for each individual azimuth direction in Figure 4.

%%%%%% Figure 3 %%%%%%

%%%%%% Figure 4 %%%%%%

Figure 4 shows the expanded energy-time spectrograms for light ions (mass channels 10-31, which correspond proton and alpha particle for the energy range 3-8 keV/q) organized by azimuthal sector during (a) 0605:00-0608:20 UT and (b) 0621:00~0624:20 UT. In the both time periods, the intense counts centered at 7th elevation (El=7), third azimuth (Az=3) are the solar wind alpha particles of about 4 keV/q (solar wind protons are about 2 keV and are outside the energy range of Figure 4). The other intense counts seen at southward looking elevation direction (El=13~15) at around 4~6 keV/q (2~3 times the solar wind proton energy, marked by arrows) are protons according to the mass analyser (not shown here). These intense proton counts are recognized over several azimuthal sectors (Az=1, 2, 3, 4 for the both time periods), and are most likely of ring ions that have originated from the same velocity (e.g., $\mathbf{V}_0$ = 0) as analyzed later.

There is a difference in the elevational extent of these counts between these two time periods: the counts are registered in only one or two elevation directions during the first time period whereas they are registered in several elevation directions during the second time period. The difference indicates that the IMF direction is slightly different between these periods. In fact the registered directions and energies of these ring-like counts (extra counts other than solar wind) vary time to time in Figure 3 from the bow shock crossing (~0551 UT) until these extra counts disappear at around 0633 UT, indicating that the IMF direction is changing.

%%%%%% Figure 5 %%%%%%

The actual selected set of data used in our analysis is listed in Table 1 for the first period (~0608 UT) and in Table 2 for the second period (0623~0624 UT). In both Tables, the first three columns are the elevation scan number (El), azimuthal sector number (Az), and center energy (keV) of the energy step in which the ring-like protons are detected. The next three columns are the corresponding velocity components (km/s) in MSO coordinates, followed by the observed counts in the proton channel. From these data, one can obtain the maximum, medium, and minimum variance directions (**L**, **M**, **N**). The velocity in the solar wind frame (subtracted by $\mathbf{V}_{SW}$ (599.6 km/s in -X direction)) along the **L**, **M**, **N** vectors are shown in the last three columns of Tables 1 and 2. The transformed data (to LMN coordinate) are plotted in Figure 5a and Figure 5b, respectively. In Figure 5, each cluster of points is enveloped by dashed circle, and the highest count registered within each cluster is given at each dashed circle (summation of two highest counts is given inside the parenthesis).

4.1. 0608 UT

Table 1. Selected ring counts at around 0608 UT, 3 June 2005.

El	energy	V_X	V_Y	V_Z	count	V_L *1	V_M *2	V_N *3

Az	(keV)	(km/s)	(km/s)	(km/s)		(km/s)	(km/s)	(km/s)
13 01	4771	-711	-410	485	153	-341	-401	372
13 01	4352	-679	-391	464	296	-324	-362	371
14 01	5712	-728	-422	616	15	-336	-495	466
14 01	5225	-696	-404	590	14	-320	-453	461
15 01	5712	-671	-392	696	7	-291	-497	558
13 02	4771	-810	-106	492	13	-46	-470	272
14 02	5225	-793	-106	596	36	-31	-521	363
14 02	4771	-758	-102	569	176	-28	-476	363
14 03	5225	-769	205	602	14	280	-492	336
14 03	4771	-734	196	575	11	269	-449	338
15 03	4771	-677	179	647	27	265	-448	431
15 03	4352	-647	171	618	8	255	-406	428
14 04	4352	-572	442	554	71	517	-297	383

*1) **L** = (0.06, 0.99, 0.14) in MSO
*2) **M** = (0.79, 0.04, -0.61) in MSO
*3) **N** = (0.61, -0.15, 0.78) in MSO

The minimum variance method on Table 1 data gives a linear alignment in the V_L-V_M plot, and a concentrated scatter in the V_N-V_M plot, as shown in Figure 5a. V_L ranges from -340 km/s to + 520 km/s while scatter in V_M and V_N is very small. The maximum variance direction **L** is pointing in the Y direction with very small $L_X = 0.06$ (corresponding 3° offset from ideal orientation). Therefore, **L** is most likely aligned to $\pm\mathbf{E}_{SW}$ direction, and hence, $\mathbf{B}_T$ is oriented in $\pm(0, -L_Z, L_Y) = \pm(0, -0.14, 0.99)$ direction, i.e., nearly north-south aligned with only a -10° tilt toward +Y ($B_Y/B_Z < 0$) in MSO. Since V_M and V_N are nearly constant for the entire selected data, we expect large uncertainty in the **M** and **N** directions as discussed in the previous section. One may also recognize that the count registered within each cluster monotonically decreases from left (low V_L value) to right (high V_L value) in Figure 5a.

The IMF tilt angle (θ in Figure 1) is estimated by two methods under the assumption of $|V_0| << |V_{SW}|$. One is the angle between $\mathbf{V}_{SW}$ and the highest energy direction. Peak counts of each cluster in Figure 5a is registered, from left to right in the V_L-V_M plot, at 4.4~4.7 keV for the first cluster (Az=1), 4.8~5.2 keV for the second cluster (Az=2) and third cluster (Az=3), and 4.4 keV for the last direction (Az=4) according to Table 1. If we take the second cluster's directions, θ is about +37° ($B_X/B_Z > 0$) in MSO.

The second method to derive θ is using the energy ratio between the highest energy (4.8~5.2 keV) and the solar wind proton energy (2 keV), which is about 2.4~2.6. This energy ratio leads to θ = ±36~39°, in good agreement with the first method of estimating the tilt angle. The agreement suggests the rational of the $|V_0| << |V_{SW}|$ assumptions, and hence the tilt angle θ is most likely about +35~+40° ($B_X/B_Z > 0$). The minimum variance direction **N** happens to give about +40° tilt toward X and -10° tilt toward Y, but this is just a coincidence because the uncertainty in the **M** and **N** directions is very large as mentioned above.

4.2. 0623 UT

The minimum variance method on Table 2 data gives a half circle in the V_L-V_M plot and a linear alignment in the V_N-V_M plot, as shown in Figure 5b. Therefore, the **N** direction, which is (0.30, -0.47, 0.83) in MSO, is a good estimate of the IMF orientation. The ring paths through zero velocity in Martian frame, indicating that the ring is originated from newly ionized hydrogen atoms with $|V_0| << |V_{SW}|$. The estimated IMF orientation is still mainly in north-south direction, tilting from north about 30° toward dawn ($B_Y/B_Z < 0$), and +18° toward Sun ($B_X/B_Z > 0$) during this second period. The direction is slightly different from the first period. On the other hand, one may again recognize a monotonic decrease in counts registered in each cluster from left (low V_L value) to right (high V_L value) in Figure 5b.

Table 2. Selected ring counts at around 0623 UT, 3 June 2005.

El Az	energy (keV)	V_X (km/s)	V_Y (km/s)	V_Z (km/s)	count	V_L *1 (km/s)	V_M *2 (km/s)	V_N *3 (km/s)
9 01	6245	-940	-531	154	5	-495	-315	277
9 01	5712	-899	-508	147	146	-466	-278	273
9 01	5225	-860	-485	141	15	-439	-242	269
10 01	6245	-922	-523	259	47	-441	-340	366
10 02	6245	-1049	-130	267	8	-129	-502	150
11 02	7446	-1112	-140	404	162	-100	-610	249
12 02	6245	-977	-126	468	16	-24	-514	336
12 02	5712	-934	-120	448	19	-16	-467	329
13 02	5712	-886	-116	538	4	37	-459	416

14 02	5712	-829	-111	623	4	90	-440	501
12 03	5712	-906	247	455	13	315	-483	170
13 03	6245	-898	242	570	41	360	-520	270
14 03	5712	-804	215	629	17	385	-454	360
14 03	5225	-769	205	602	15	375	-410	352
15 03	4771	-677	179	647	23	395	-341	430
15 04	3978	-504	387	595	8	603	-184	339
13 05	2267	-274	485	349	9	652	111	157
13 05	2051	-261	461	332	7	629	133	158
14 05	1519	-210	370	329	5	562	190	214
14 05	1371	-199	352	312	5	542	208	219

*1) **L** = (0.27, 0.87, 0.40) in MSO
*2) **M** = (0.92, -0.11 -0.39) in MSO
*3) **N** = (0.30, -0.47, 0.83) in MSO

Let us examine the new method in deriving the IMF orientation for this ideal case. The maximum variance direction is obtained as **L** = (0.27, 0.87, 0.40) in MSO. If we remove the lowest energy direction (all points with $V_M > 0$) according to the procedure (3) in section 3, we have **L** = (-0.05, 0.87, 0.50) which gives mainly north-south oriented $\mathbf{B}_T$, tilting from north to toward dawn about 30° ($B_Y/B_Z < 0$). The highest energy direction at the second cluster from the left in the V_L-V_M plot (7.4 keV, Az=2) gives $\theta = +21°$ ($B_X/B_Z > 0$), while the energy ratio (about 3) gives about a ±15° tilt angle toward X from north-south orientation. The estimated IMF orientation by the new procedure is the same the **N** direction.

4.3. 0614 UT

Table 3. Selected ring counts at around 0614 UT, 3 June 2005.

El Az	energy (keV)	V_X (km/s)	V_Y (km/s)	V_Z (km/s)	count	V_L *1 (km/s)	V_M *2 (km/s)	V_N *3 (km/s)
1001	3978	-736	-417	207	5	-159	407	-211
1001	3627	-702	-398	197	14	-151	393	-175
1101	4352	-746	-425	302	54	-99	478	-236
1101	3978	-714	-407	289	46	-94	461	-199
1201	4772	-750	-429	403	9	-32	551	-253
1201	4352	-716	-410	385	46	-30	531	-215
1301	4772	-711	-410	485	22	40	603	-224
1301	4352	-679	-391	464	22	38	581	-187
1302	4352	-773	-101	470	7	251	371	-246
1402	5225	-793	-106	596	23	335	460	-282

1502	4352	-667	-92	613	16	358	485	-159
1502	3978	-638	-88	586	9	342	468	-126

*1) **L** = (0.01, 0.72, 0.69) in MSO
*2) **M** = (0.18, -0.68, 0.71) in MSO
*3) **N** = (0.98, 0.12, -0.13) in MSO

In Figure 3, the ring-like protons in the energy range 3~8 keV (protons most likely having zero initial velocity) is visible until 0631 UT, beyond which the ring-like protons suddenly disappear (at around 0633 UT). Since it is impossible that the proton source (hydrogen corona) suddenly disappear at this distance from Mars, this disappearance must be caused by changes in the IMF direction, such that the ring plane becomes to tilt out of IMA's field of view. That means that $|\theta| > 40°$ after 0633 UT. Thus, the IMF direction varied dynamically during 0608-0634 UT.

In fact, at 0614 UT when we find a weak ring signature at low energy as listed in Table 3 (the format is the same as Tables 1 and 2), the IMF orientation is not a simply interpolated direction from orientaions at 0608 UT and 0623 UT. Applying the present method to the Table 3 data (corresponding LMN plot is shown in Figure 5c), θ is estimated about +40° ($B_X/B_Z > 0$) with about a -45° tilt from +Z toward +Y ($B_Y/B_Z < 0$). The decrease in registered counts is again recognized from low V_L value to high V_L value in Figure 5c.

4.4. Monotonic change in count

In all three periods in which we could safely estimate the IMF orientation from the proton ring distribution, the registered counts monotonically decreased from low V_L value to high V_L value, with the **L** directions pointing in similar directions (15°~35° angles between different periods) in MSO coordinate. Note that there are many observations of ring distributions which are symmetric in the V_L direction (Paper 1). The IMF orientations for such ideal (non-change) cases are stable.

Since no consecutive full scan (192 sec apart) repeats the same ring distribution in Figure 3, the IMF orientation changed between different elevation scans (192 sec cycle). Therefore, it is possible that the IMF orientation slightly fluctuated within a gyroperiod (with is about 13 sec for 5 nT magnetic field). In a fluctuating magnetic field, the phase-space density of ions within the ring decays from its highest value at $\mathbf{V} = \mathbf{V}_0$ (=0) because the selected ring ions (Tables 1, 2, and 3) are originated only from newly ionized hydrogen atoms with $|V_0| << |V_{SW}|$ (cf. section 4.2 and Paper 1). In fact, the old ring ions disappear every 192 sec cycle. It is impossible to attribute the observed monotonic change in the $+V_L$ direction count as a growth of the ring distribution because there is no other intense ion source than the newly ionized atoms at this energy range (2~6 keV/q).

Before we attribute the decrease of count to decay, we should consider the time resolution of the observation because each elevation step takes 12 sec for a complete energy sweep. The time resolution is comparable to a gyroperiod for 5 nT magnetic field, and hence the flux change in the elevation direction might be attributed to the temporal change in the degree of scattering decay. However, the monotonic decrease is seen in the azimuthal direction in Table 1 (Figure 5a), which is simultaneously observed. Furthermore, all three cases shows the monotonic decrease in the same direction in space. These facts strongly suggest that the common monotonic decrease in registered count toward $+V_L$ direction can be attributed to the short-time scattering decay during a single gyration. This explains why we do not often observe double or triple ring directions in Figures 3 or 4. If the decay takes more than one gyroperiod, we should be able to observe different rings at the same energy range very often.

In summary, the common decrease in count in the $+V_L$ (or $+V_Y$) direction in Figure 5 (or Tables 1, 2, and 3) most likely represents decay of the distribution during the gyromotion (e.g., due to changing IMF). If so, +**L** (and hence +**Y**) points toward the decay direction at the highest energy point of the ring (corresponding to point between "3" and "4" in Figure 1), and hence, $\mathbf{E}_{SW}$ points toward the -**Y** (dusk-to-dawn) direction. This corresponds to a northward pointing $\mathbf{B}_T$, while the positive θ means a sunward pointing B_X (>0).

4.5. Summary

Table 4. Estimated IMF direction on 3 June 2005.

UT	alignment	Tilt toward +X (θ)	Tilt toward +Y	polarity
0608	north-south	~ +35~40° (sunward)	~ -10° (dawnward)	$B_Z > 0$
0613	north-south	~ +40° (sunward)	~ -45° (dawnward)	$B_Z > 0$
0623	north-south	~ +20° (sunward)	~ -30° (dawnward)	$B_Z > 0$
0633~	?	$\|\theta\| > 40°$	?	(B_Z>0?)

The estimated IMF directions at around 0608 UT, 0613 UT, 0623 UT, and 0633-0643 UT are summarized in Table 4. In the third and fourth columns, the tilt angle is given from +Z alignment, and the sign of directions (sunward and dawnward) is given according to the sign of IMF (B_Z in the present case) polarity that is estimated in subsection 4.4.

5. Discussion.

Let us compare our result in Table 4 with the estimated IMF from MGS magnetometer data (Acuna et al., 1998; Fedorov et al., 2006). For a better estimate of IMF from the 400km circular orbit of MGS, Frilund et al. (2008) applied a hybrid simulation

prediction of the MGS magnetic field data. They tried to find the best-fit constant IMF that reproduces the MGS magnetic field observations during a 10 min duration (i.e., from subsolar region to the northern polar region). This hybrid-plus-MGS model predicts the IMF orientation as (-0.57, 0.20, 0.79), i.e., the IMF points mainly northward with about -35° tilt toward X and +10° tilt toward Y.

The orientation of estimated $\mathbf{B}_T$ (north-south oriented) is similar between the present estimate and the hybrid-plus-MGS model at 0608 UT. Furthermore, the changing direction of $\mathbf{B}_T$ (increasing tilt angle toward dusk) obtained here is actually observed in MGS magnetic field data (Frilund et al., 2008, Figure 3). Note that the hybrid model assumes a constant IMF, while the estimated IMF by the IMA data changes rather quickly as discussed in section 4. On the other hand, IMF tilt angle from north-south orientation is quite different between the present estimate ($B_X/B_Z > 0$) and hybrid-plus-MGS model ($B_X/B_Z < 0$). This difference indicates that the magnetic piling effect at the ionopause is quite strong at the MGS altitude, and that the IMF B_X component derived from the MGS data might have large uncertainty.

The sign of the IMF direction estimated in section 4.4 (mainly northward) is also the same as that obtained from the MGS observation, supporting our method although one may still claim this as a coincidence. We could estimate the sign because of quick temporal variation. This explains why we could not identify clear sets of ring data for most of the presented period except at 0608 UT, 0613 UT, and 0623 UT. In Paper 1 where we could not estimate the sign of IMF, the ring distributions did not decay for more than several elevation scan cycles (> 10min). Such rather stable ring distribution is often observed when the ring plane's orientation is stable. Inversely, when the IMF direction varies quickly, the ring distribution may decay quickly, giving us a clue in determining the evolution direction of the ring distribution and hence the sign of the IMF.

The dynamic change in the IMF direction indicates that the bow shock might switch between a quasi-parallel shock and a quasi-perpendicular shock. Such a switch in the property of the shock is expected to be observed in the electron signature because the travel time of foot electrons along the magnetic field is only a few seconds over the distance from the bow shock to the spacecraft (a 30 eV electron travels about 1 R_M/s). When the IMF points mainly northward, the dawn side bow shock is expected to be a quasi-perpendicular shock, for which the foreshock foot region does not extend beyond an ion gyro radius. When the tilt of the IMF toward dusk becomes large (e.g., 0613 UT), the bow shock might start behaving like a quasi-parallel shock, for which the foreshock foot region extends to many R_M.

In Figure 3, ELS sector-08 is viewing electrons traveling along the +B projection direction (viewing electrons from the field line foot region), and we see a clear drop of energy flux of electrons within the energy range between 10 eV and 300 eV around

0608 UT and 0623 UT compared to other periods between 0608 UT and 0640 UT. This is consistent with the IMF orientation derived in this paper, i.e., the IMF orientation that clearly makes the bow shock the quasi-perpendicular is found at only 0608 UT and 0623 UT. Thus, the variation of the IMF tilt angle from north inferred from the IMA data is consistent with the electron data.

6. Conclusions

Our previous method of deriving the IMF orientation from MEX/IMA data (Paper 1) is further improved to derive the IMF orientation from very limited part of ring distributions, i.e., only the highest energy portion of the ring distribution. This method uses the maximum variance direction **L** derived from manually selected ring data. Because IMA's count rate is nearly proportional to the differential energy flux density, i.e., to energy squire for a semi-persistent ring distribution, **L** is most likely parallel to the tangential direction of the ring distribution at its highest energy, where this tangential direction is parallel or anti-parallel to the electric field. Therefore, $\pm(0, -L_Z, L_Y)$ is a good estimate of orientation of $\mathbf{B}_T$, the component of IMF in the Y-Z plane in MSO (perpendicular to the solar wind).

The tilt angle of the IMF toward the +X direction from +Z orientation (θ in Figures 1 and 2) is determined by two different methods when the initial velocity of the ring ions ($|\mathbf{V}_0|$) is small compared to the solar wind velocity ($|\mathbf{V}_{SW}|$). The first is given by the angle between the highest energy direction of the ring and the -X direction, and the second is given by the energy ratio between the highest energy of the ring protons and the energy of the solar wind protons. If both method give a same θ value, $|\mathbf{V}_0|$ is most likely small compared to $|\mathbf{V}_{SW}|$ and the obtained θ is most likely reliable. Finally, even the sign of the IMF direction can be determined if one can estimate the evolution direction of the ring distribution. The present example shows such a case.

The actual procedure, with quality control, is given with 6 steps (1)-(6) at the end of section 3. We have applied this method to the IMA data for three periods (at around 0608 UT, 0613 UT, and 0623 UT) outside the bow shock on 3 June 2005. For all three periods, we obtained mostly north-south orienting IMF directions, with some tilt from north toward +X and -Y as summarized in Table 4. The tilt angle both toward X (θ) and toward Y changes time to time, indicating that the ring distribution may decay during a gyration due to the fluctuation IMF direction. From the monotonic decrease of count in one direction in MSO coordinate, we also estimated the sign on IMF direction as $B_Z>0$. The northward oriented IMF is in good agreement with the MGS magnetic field observation at 400 km from Mars, which was projected into the solar wind by a hybrid simulation.

Acknowledgement

The Mars Express mission is the first European mission to the red planet managed by the European Space Agency (ESA). The ASPERA-3 experiment on the Mars Express mission is a joint effort between 15 laboratories in 10 countries, all sponsored by their national agencies. We thank all these agencies as well as the various departments/institutes hosting these efforts. ASPERA-3 experiment main PI work is supported by the Swedish National Space Board, while ELS instrument work is supported by National Aeronautics and Space Administration (NASA) contract NASW-00003 in the United States. Yamauchi thanks to programs for disabled people in Sweden, which have made it possible for him to work.

References

Acuña, M.H., Connerney, J.E.P., Wasilewski, P., Lin, R.P., Anderson, K.A., Carlson, C.W., et al., 1998, Magnetic field and plasma observations at Mars : preliminary results of the Mars Global Surveyor mission, Science, 279 (5357), 1676-1680.

Barabash, S., Lundin, R., Andersson, H., Brinkfeldt, K., Grigoriev, A., Gunell, H., Holmström, M., Yamauchi, M., Asamura, K., Bochsler, P., et al. (2006), The analyzer of space plasmas and energetic atoms (ASPERA-3) for the Mars Express mission, Space Sci. Rev., 126(1-4), 113-164, doi: 10.1007/s11214-006-9124-8.

Fedorov, A., Budnik, E., Sauvaud, J.-A., Mazelle, C., Barabash, S., Lundin, R., et al., 2006, Structure of the Martian wake, Icarus, 182(2), 329-336, doi:10.1016/j.icarus.2005.09.021.

Frilund, H., Kallio, E., Yamauchi M., Fedorov, A., et al. (2008), The Magnetic Field Near Mars: A Comparison Between A Hybrid Model, Mars Global Surveyor and Mars Express Observations, Planet. Space Sci., in press.

Lundin, R., Barabash, S., Andersson, H., Holmström, M., Grigoriev, A., Yamauchi, M., et al., 2004, Solar wind-induced atmospheric erosion on Mars: First results from ASPERA-3 on Mars Express, Science, 305, 1933-1936.

Sckopke, N., Paschmann, G., Brinca, A.L., Carlson, C.W., and Luhr, H., (1990), Ion thermalization in quasi-perpendicular shocks involving reflected ions, J. Geophys. Res., 95, 6337-6352.

Sonnerup, B.U.O., and Scheible, M., (1998), Minimum and maximum variance analysis, in Analysis Methods for Multi-Spacecraft Data, edited by Paschmann, G. and Daly, P.W., ISSI scientific report, ESA publications division, Noordwijk, The Netherlands.

Vignes, D., Mazelle, C., Rème, H., Acuña, M.H., Connerney, J.E.P., Lin, R.P., Mitchell, D.L., Cloutier, P., Crider, D.H., and Ness, N.F. (2000), The Solar Wind interaction with Mars: locations and shapes of the Bow Shock and the Magnetic Pile-up Boundary from the observations of the MAG/ER experiment onboard Mars Global Surveyor, Geophysical Research Letters, Volume 27(1), 49-52.

Yamauchi, M., Futaana, Y., Fedorov, A., Dubinin, E., Lundin, R., Sauvaud, J.-A., Winningham, D., Frahm, R., Barabash, S., Holmström, M., Woch, J., Fraenz, M., Budnik, E., Borg, H., Sharber, J.R., Coates, A.J., Soobiah,Y., Koskinen, H., Kallio, E., Asamura, K., Hayakawa, H., Curtis, C., Hsieh, K.C., Sandel, B.R., Grande, M., Grigoriev, A., Wurz, P., Orsini, S., Brandt, P., McKenna-Lawler, S., Kozyra, J., and

624 Luhmann, J. (2006), IMF direction derivation from cycloid-like ion distributions
625 observed by Mars Express, Space Sci. Rev., 126(1-4), 239-266, doi:10.1007/s11214-
626 006-9090-1, 2006.
627 ---
628 Correspondence: M. Yamauchi, Swedish Institute of Space Physics, Box 812, S-98128
629 Kiruna, Sweden, phone: +46-980-79050, fax: +46-980-79120, Email:
630 M.Yamauchi@irf.se
631

631

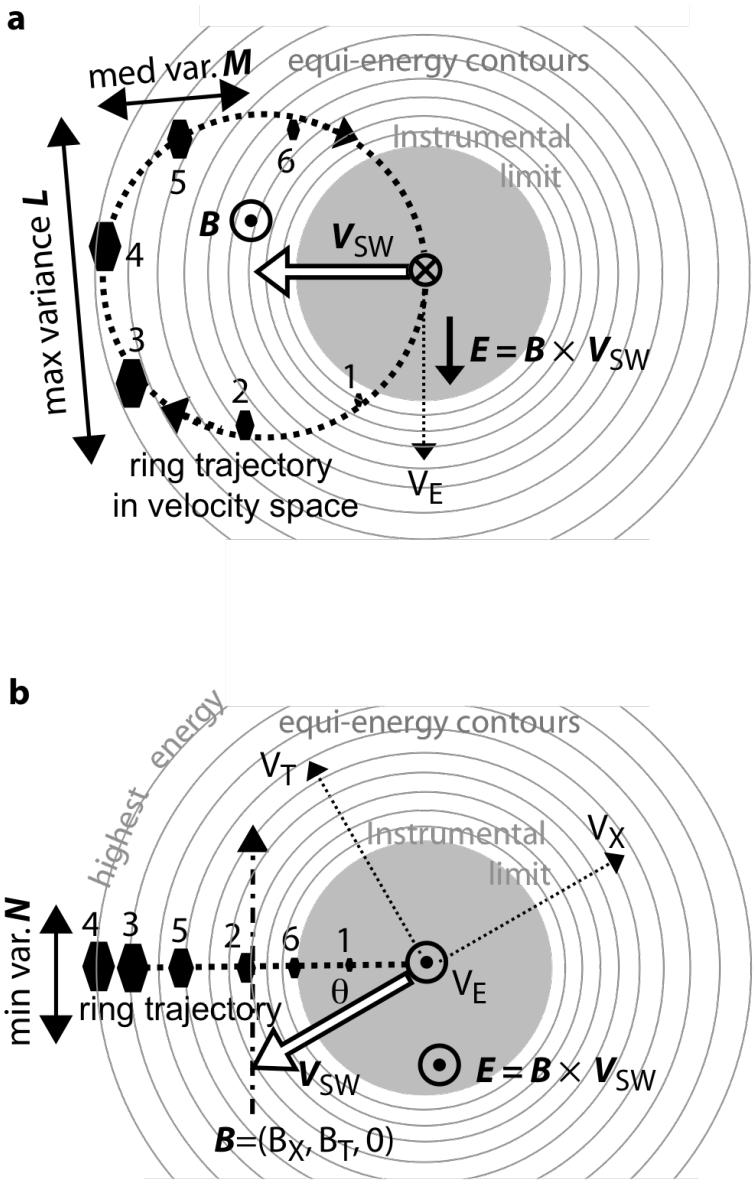

632

633 **Figure 1:** Illustration of velocity space trajectory (thick dashed circle/line) of newly
634 ionized hydrogen corona in the solar wind. (a) The upper panel: the top view from +**B**.
635 (b) The lower panel: the side view (from $+\mathbf{E}_{SW} = -\mathbf{V}_{SW} \times \mathbf{B}$). See text for the definition
636 of the Martian frame Cartesian coordinates (V_X, V_T, V_E). The thin circles are the equi-
637 energy lines, which represent the detection energy steps of the instrument (which is in a
638 logarithmic scale: only every other energy steps of IMF are drawn for the relevant
639 energy range), and the round shaded area is undetectable by IMA proton measurements
640 (see text). Ions with $\mathbf{V}_0 = 0$ in the Martian frame have an initial velocity of $-\mathbf{V}_{SW}$ in the
641 solar wind frame where the electric field disappears, and they gyrate about **B** with a
642 constant parallel velocity to **B**. In velocity space, this motion forms a circle with a
643 radius $|V_{SW}| \cos(\theta)$, where $\sin(\theta) = B_X/|B|$, i.e., θ is an angle between **B** and the V_T axis
644 (see the lower panel). The hexagonal marks denote directions from Martian frame
645 origin with 22.5° angular resolution (corresponds to azimuthal resolution of IMA),
646 while its size represents the expected counts which is nearly proportional to energy
647 squire for a semi-persistent ring distirbution (see text). The hexagonal marks are

numbered in time sequence. The expected maximum, medium, and minimum variance directions (**L**, **M**, **N**, respectively) of this asymmetric data are expected to be orientated as illustrated by the double arrows.

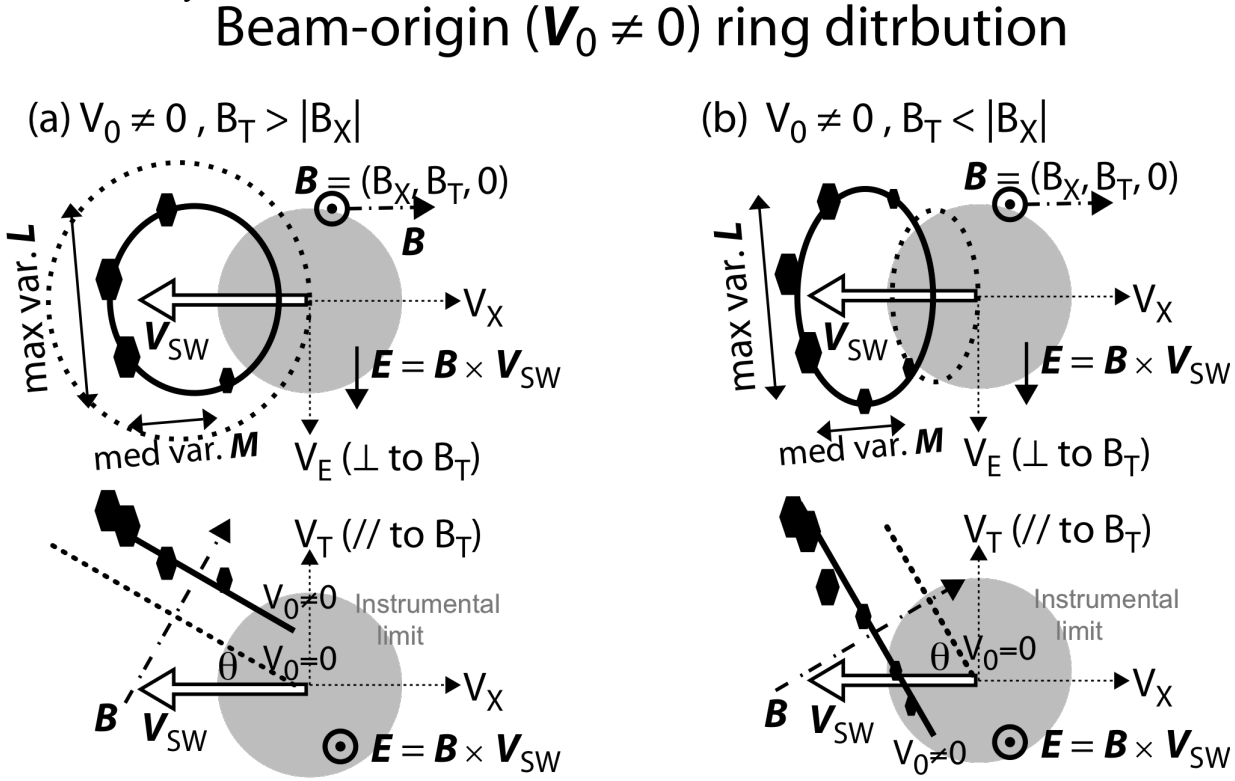

Figure 2: Illustration of velocity space trajectory (thick circle/line) of beam-origin ions ($\mathbf{V}_0 \neq 0$ in the Martian frame) in the solar wind. For reference, the trajectory for ions with $\mathbf{V}_0 = 0$ is also shown with thick dashed circle/line. Two types of IMF conditions, (a) $|B_X| < B_T$, and (b) $< |B_X| > B_T$ (≥ 0), are illustrated although there is no physical difference between these cases. Format is the same as Figure 1 except that the view is tilted by an angle θ such that the X direction points toward the right for both the upper and lower panels. The projection of the ring distribution onto the V_X-V_E plane forms an ellipse with the short/long radius ratio cos(θ). The radius of the ring distribution is different between the $\mathbf{V}_0 \neq 0$ cases and $\mathbf{V}_0 = 0$ case.

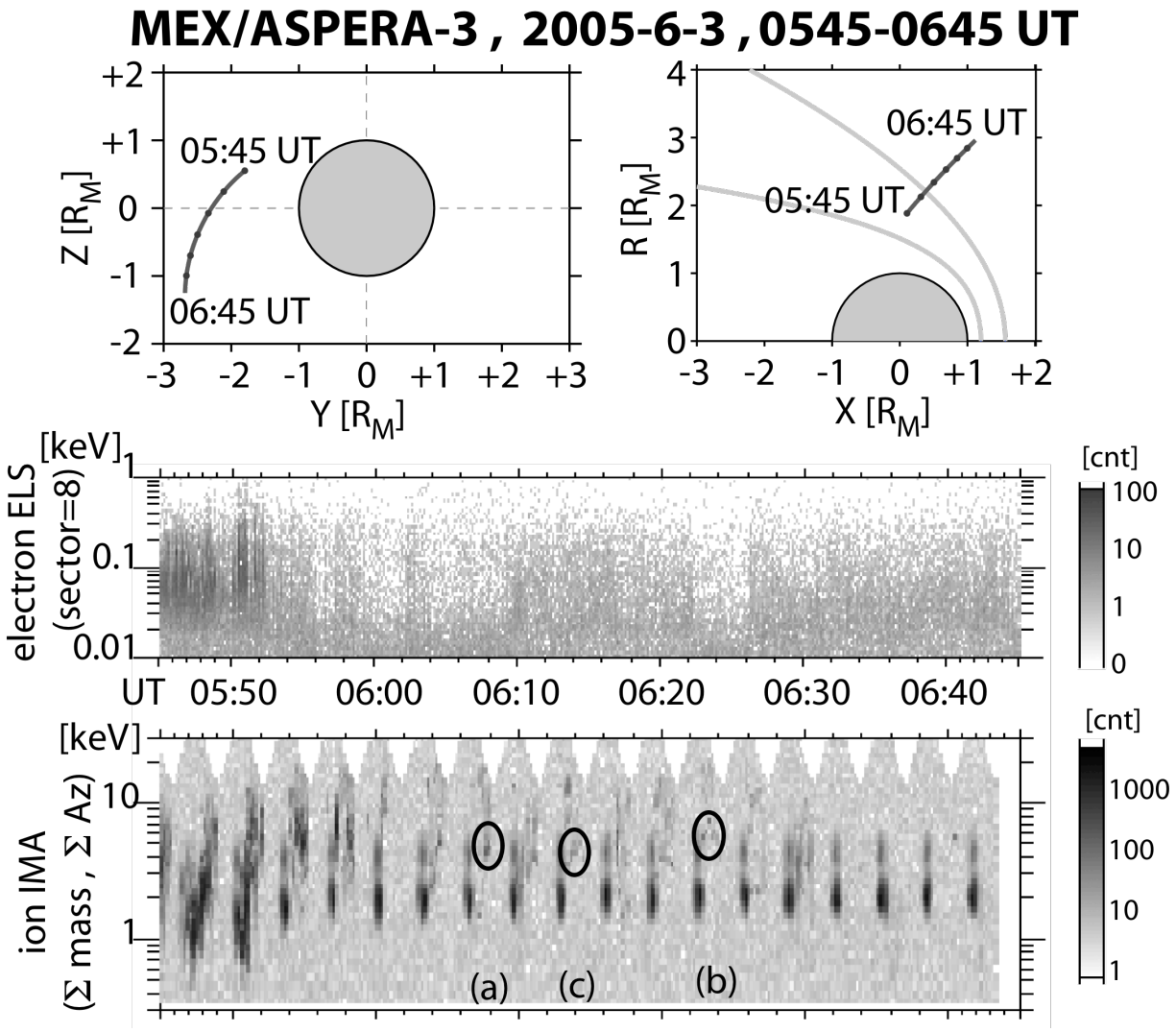

662
663 **Figure 3:** Overview of the MEX orbit and hot plasma data during 0545-0645 UT on 3
664 June 2005. The upper plots show the MEX orbit in the MSO coordinate system (see
665 text for definition). The unit "R_M" is the Martian radius (3397 km). The average
666 boundary positions (bow shock and induced magnetosphere boundary (Vignes et al.,
667 2000)) are drawn with grey lines in the upper right panel. The MEX traversal (IMA
668 operational) is drawn by a thick line. The lower panels show the energy-time
669 spectrograms of electrons (from ELS, 10 eV ~ 1 keV) and ions (from IMA, 0.3~30
670 keV/q). For IMA, all mass and azimuthal angles are integrated, while only sector=8 is
671 presented for ELS. The nearly 3-min (192 sec) cycle seen in the IMA data is due to the
672 scanning cycle of the IMA entrance direction from elevation=0 to elevation=15. During
673 this period, elevations 0 and 15 are looking about 40° northward and about 40°
674 southward from the equatorial plane, respectively, and the solar wind protons (about 2
675 keV/q) and alpha particles (about 4 keV/q) are seen at elevation 6~8. In addition to the
676 solar wind, one can recognize counts at > 3 keV/q at elevation=10~15, but not at
677 elevation=0~5. Low energy part of these extra counts (marked by circles) is the best
678 candidate for the ring distribution with zero initial velocity (see text). The labels (a),
679 (b), and (c) under the circle marks correspond to Tables 1, 2, and 3, respectively.

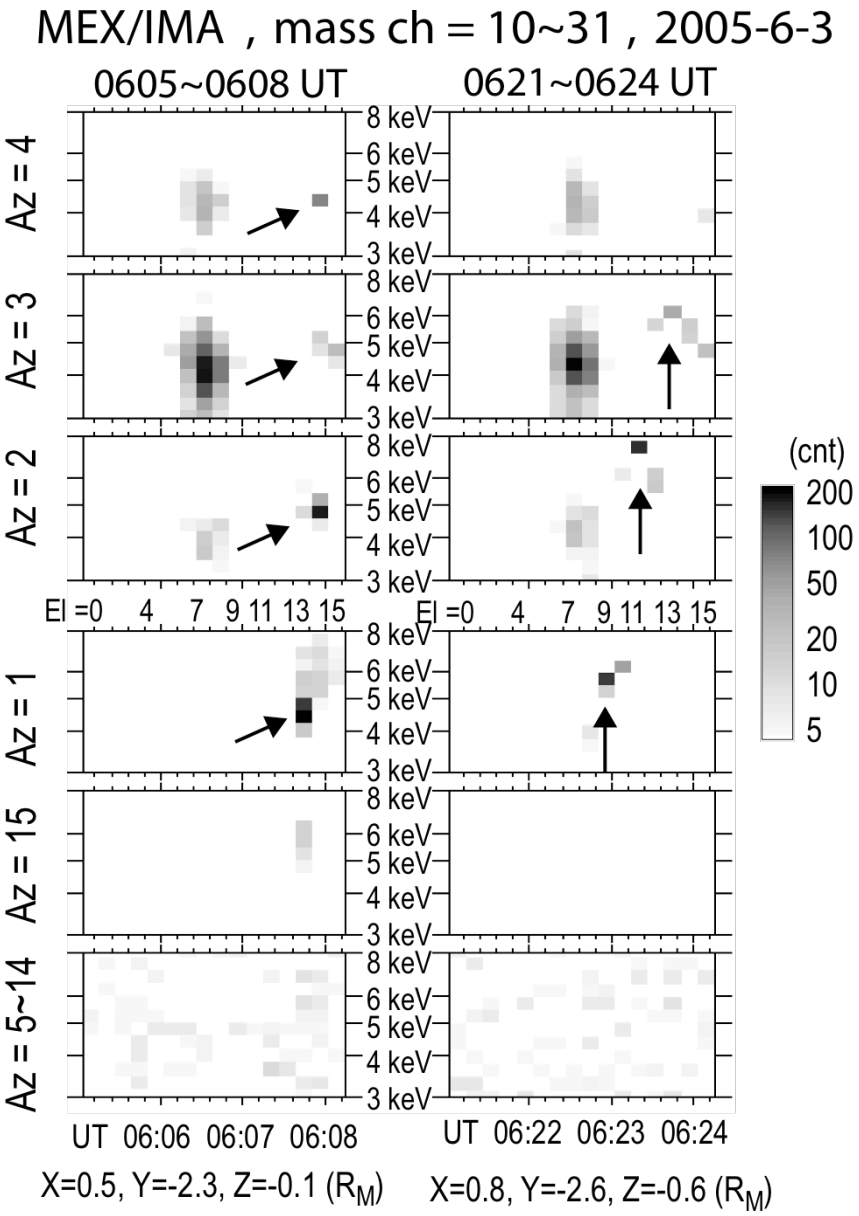

680
681 **Figure 4:** Energy-time spectrograms from IMA channels for proton and alpha particle
682 between 3 and 8 keV/q during complete elevation scans at (a) 0605:00-0608:20 UT and
683 (b) 0621:00-0624:20 UT from the same period shown in Figure 3. Six different
684 azimuthal sectors (from top 4, 3, 2, 1, 15, and integration over 5-14) are presented.
685 Sector 0 is not presented because it gathers contamination from all of the other sectors.
686 The first pixels of each spectrograms (the leftmost pixels) correspond to elevation=0
687 (El=0: looking about +40° (northward) from the equatorial plane during this event) and
688 the last pixels (the rightmost pixels) to elevation=15 (El=15: looking about -40°
689 (southward) from the equatorial plane during this event). The solar wind alpha
690 particles of about 4 keV/q (i.e., 8 keV with q=2) are seen at elevation=6~8. The ring-
691 like ions seen at elevation=11~15 (marked by arrows) are lighter than these alpha
692 particles according to the mass analyser (not shown here), and hence they are protons.

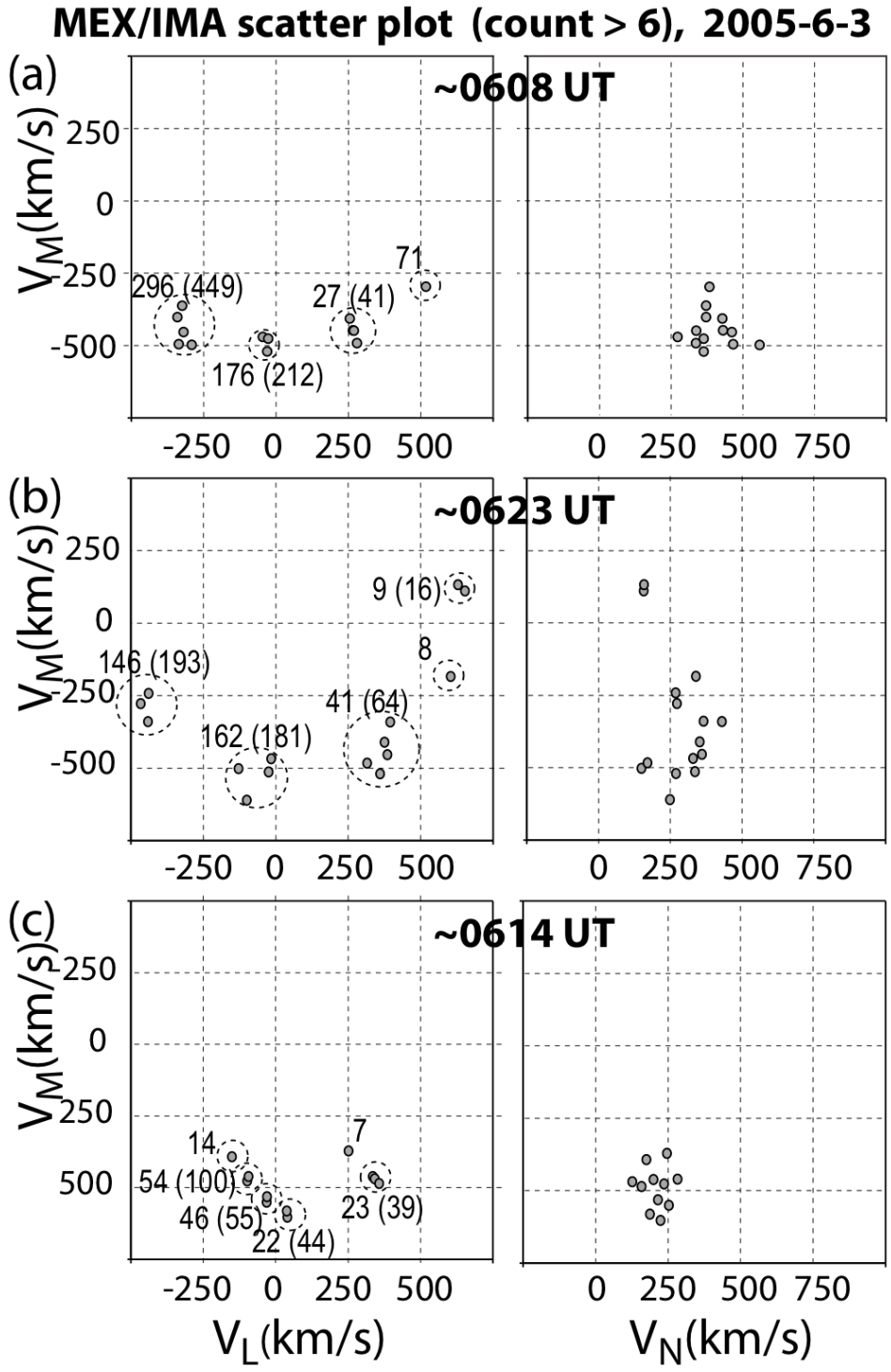

Figure 5: Velocity scatter plots of the selected ring-like protons in the solar wind frame for all three cases that are given in Table 1 (~0608 UT), Table 2 (~0623 UT) and Table 3 (~0614 UT) on 3 June 2005. The local LMN (minimum variance) coordinates are given at the bottom of each table. The velocity space points with count more than 5 are plotted. The number given at each cluster of points (each cluster is enveloped by dashed circle) is the highest count that is registered within each cluster, with summation of two highest counts given inside the parenthesis.